Cell Research

www.nature.com/cr
www.cell-research.com

ARTICLE

Structure of human RNA polymerase III elongation complex

Liang Li[1], Zishuo Yu[1], Dan Zhao[1], Yulei Ren[1], Haifeng Hou[1] and Yanhui Xu[1,2,3,4]

RNA polymerase III (Pol III) transcribes essential structured small RNAs, such as tRNAs, 5S rRNA and U6 snRNA. The transcriptional activity of Pol III is tightly controlled and its dysregulation is associated with human diseases, such as cancer. Human Pol III has two isoforms with difference only in one of its subunits RPC7 (α and β). Despite structural studies of yeast Pol III, structure of human Pol III remains unsolved. Here, we determined the structures of 17-subunit human Pol IIIα complex in the backtracked and post-translocation states, respectively. Human Pol III contains a generally conserved catalytic core, similar to that of yeast counterpart, and structurally unique RPC3–RPC6–RPC7 heterotrimer and RPC10. The N-ribbon of TFIIS-like RPC10 docks on the RPC4–RPC5 heterodimer and the C-ribbon inserts into the funnel of Pol III in the backtracked state but is more flexible in the post-translocation state. RPC7 threads through the heterotrimer and bridges the stalk and Pol III core module. The winged helix 1 domain of RPC6 and the N-terminal region of RPC7α stabilize each other and may prevent Maf1-mediated repression of Pol III activity. The C-terminal FeS cluster of RPC6 coordinates a network of interactions that mediate core–heterotrimer contacts and stabilize Pol III. Our structural analysis sheds new light on the molecular mechanism of human Pol IIIα-specific transcriptional regulation and provides explanations for upregulated Pol III activity in RPC7α-dominant cancer cells.

Cell Research (2021) 31:791–800; https://doi.org/10.1038/s41422-021-00472-2

INTRODUCTION

Eukaryotic transcription is mediated by three classes of structurally related RNA polymerases, RNA polymerase (Pol) I, Pol II and Pol III.[1–3] Pol III is dedicated to generate transfer RNAs (tRNAs), the most abundant cellular RNAs, and other small noncoding RNAs including spliceosomal U6 small nuclear RNA (snRNA) and 5S ribosomal RNA (5S rRNA), many of which are related to the ribosome biogenesis and protein synthesis.[4,5] The transcription of these RNAs requires highly efficient transition from termination to reinitiaiton, a characteristic feature of Pol III-mediated transcription.[6,7] Dysregulation of Pol III-mediated transcription is associated with human diseases, such as cancer.[8–12]

As the largest member among the three eukaryotic RNA polymerases, Pol III has molecular weight of ~0.7 megadalton and consists of 17 subunits that are organized into a catalytic core, a peripheral stalk module, and Pol III-specific subcomplexes.[3] The catalytic core and stalk are structurally conserved across eukaryotic RNA polymerases. The Pol III-specific TFIIE-like heterotrimeric subcomplex C82–C34–C31 in yeast (equivalent of human RPC3–RPC6–RPC7) is required for transcription initiation.[13–16] The Pol III-specific TFIIF-like heterodimeric subcomplex C53–C37 (equivalent of human RPC4–RPC5) functions in transcription initiation and termination.[17–21] The yeast C11 (equivalent of human RPC10) subunit in the catalytic core has intrinsic RNA exonuclease activity for error correction and is functionally similar to TFIIS, the elongating factor of Pol II.[22–24]

Maf1 is a negative regulator of Pol III transcription activity. In yeast, Maf1 binds Brf1, an essential subunit of TFIIIB which recruits Pol III to promoter DNA, and prevents assembly of preinitiation complex (PIC).[25] Maf1 also inhibits transcription initiation through binding C34 of Pol III and blocks the active site.[26] In human cell, Maf1 interacts with Pol III through contacting subunits RPC1 and RPAC2.[27] However, how Maf1–Pol III interaction is regulated remains elusive.

Human Pol III has two isoforms with difference only in one of its subunits RPC7 (α and β). RPC7α and RPC7β are highly similar and share 46% sequence identity.[28] RPC7α is more abundant in undifferentiated cells and tumor cells, whereas RPC7β is ubiquitously expressed. Overexpression of RPC7α enhances tumor transformation, suggesting that RPC7α may regulate the role of tumor suppressor MAF1 in repressing Pol III activity. The regulatory mechanism underlying the differential expression of two isoforms of RPC7 remains largely unknown.

Previous structural studies mainly focused on yeast Pol III and elucidated the molecular mechanisms of Pol III architecture and transcription initiation.[26,29–33] Despite the highly conserved catalytic mechanism of Pol III in yeast and human systems, structural studies of human Pol III are required for understanding the human Pol III-specific regulation and mapping the human disease-related mutations in Pol III. Here, we reported the cryo-electron microscopy (cryo-EM) structures of human Pol IIIα complex in the backtracked and post-translocation states at 3.0 Å and 3.4 Å resolution, respectively. The structures reveal a

[1]Fudan University Shanghai Cancer Center, Institutes of Biomedical Sciences, State Key Laboratory of Genetic Engineering and Shanghai Key Laboratory of Medical Epigenetics, Shanghai Medical College of Fudan University, Shanghai 200032, China; [2]The International Co-laboratory of Medical Epigenetics and Metabolism, Ministry of Science and Technology of China, Department of Systems Biology for Medicine, School of Basic Medical Sciences, Shanghai Medical College of Fudan University, Shanghai 200032, China; [3]Human Phenome Institute, Collaborative Innovation Center of Genetics and Development, School of Life Sciences, Fudan University, Shanghai 200433, China and [4]State Key Laboratory of Reproductive Regulation and Breeding of Grassland Livestock, School of Life Sciences, Inner Mongolia University, Hohhot, Inner Mongolia 010070, China
Correspondence: Haifeng Hou (houhf@fudan.edu.cn) or Yanhui Xu (xuyh@fudan.edu.cn)
These authors contributed equally: Liang Li, Zishuo Yu, Dan Zhao

Received: 20 August 2020 Accepted: 6 January 2021
Published online: 5 March 2021

highly conserved catalytic cavity and structural features distinct from yeast Pol III and provide novel insights into complex assembly and regulation of human Pol III.

RESULTS

Complex assembly and structure determination

The expression cassettes of 17 Pol III subunits were merged into six modified pCAG plasmids and transiently transfected into HEK Expi293 cells. The recombinant human Pol III complex was purified to homogeneity using immunoprecipitation (protein A-tagged RPC2), followed by ion exchange (Supplementary information, Fig. S1a). The Pol III elongation complex (EC) in the absence of NTP was assembled by incubating the purified Pol III and a DNA/RNA hybrid mimicking the transcription bubble in the backtracked state.[30] The cryo-EM structure of Pol III EC was determined using single particle reconstruction and the cryo-EM map was refined to an overall resolution of 3.0 Å (Fig. 1b, c; Supplementary information, Figs. S2, S3, Table S1, and Movie S1). The map around RPC6 was relatively weak and was further improved by focus refinement (Supplementary information, Movies S2, S3). The structural model was manually built with yeast Pol III structure[30] as template. All the 17 subunits and DNA/RNA scaffold were built in the structural model except some peripheral regions (Supplementary information, Table S2) due to intrinsic flexibility.

Overall structure of human Pol III EC

The human Pol III EC adopts an overall architecture generally similar to that of yeast Pol III EC (Supplementary information, Fig. S4a, b),[30] consistent with the high sequence similarity of the core subunits and highly conserved function across species.[3] Pol III consists of a 10-subunit core formed by RPC1, RPC2, RPAC1–2, RPABC1–5 and RPC10, a stalk formed by RPC8 and RPC9, a Pol III-specific TFIIE-like heterotrimer formed by RPC3, RPC6 and RPC7, and Pol III-specific TFIIF-like heterodimer formed by RPC4 and RPC5 (Fig. 1b, c; Supplementary information, Movie S3). The cryo-EM map reveals the mimetic transcription bubble in the active center and downstream DNA duplex (Fig. 1b, c).

The cryo-EM map is relatively weak around the RNA bases and does not support unambiguous model building (Supplementary information, Fig. S7b, d). The map around phosphate groups of 6 RNA nucleotides is fairly good and the 16 bps of DNA duplex are all well-ordered. We therefore built the structural model of RNA according to the positions of the phosphate groups and the putative RNA–DNA base pairing. In the structural model, the mimetic transcription bubble contains 6 bases of synthetic RNA complementary to template DNA (Fig. 1a). The downstream DNA (16 bp) is surrounded by the active cleft, clamp, and jaws, and extends outward through the DNA entry tunnel (Fig. 1a–c). The Pol III structure likely represents a backtracked state because the nucleotide addition site is occupied by the nucleotide U^{+1} (relative to transcription start site) while the 3′-end nucleotide C^{+2} is disordered (Supplementary information, Figs. S3b, S7b, d, f).

Structure of human Pol III in the post-translocation state

We also obtained cryo-EM map of Pol III using a DNA–RNA hybrid, the design of which has been widely used in generating Pol II EC in the post-translocation state (Supplementary information, Fig. S2). The cryo-EM map around RNA bases supports the placement of three RNA nucleotides ($A^{-3}U^{-2}C^{-1}$) according to the positions of the phosphate groups and the putative RNA–DNA base pairing (Supplementary information, Figs. S2k, S7c, e). As expected, the nucleotide addition site is empty and placed next to the 3′-end nucleotide C^{-1} (Supplementary information, Fig. S7c, e, f). Structural alignment of nucleic acids of Pol III in the backtracked and post-translocation states with yeast Pol III (PDB code: 5FJ8)[30] in the pre-translocation state shows that the RNA is tilted towards bridge helix, consistent with the conformational differences of Pol II in backtracked and elongation states[34] (Supplementary information, Fig. S7g, h). The Pol III in the two states adopt almost identical conformation (Supplementary information, Figs. S2, S7a), consistent with highly conserved structural features of Pol II in distinct translocation states.[35] The structure in the backtracked state was used in the following analyses.

The Pol III catalytic cavity is highly conserved in yeast and humans

Previous structural studies of Pol I, Pol II and Pol III indicate high similarity of the active center.[1] The "metal A" magnesium cation is coordinated by side chains of three conserved aspartate residues (D499, D501, D503) of RPC1 and binds to the growing RNA 3′ end (Supplementary information, Fig. S3b). The nucleic acid-binding residues are mainly from core subunits RPC1, RPC2 and RPABC1. Most of these residues are invariant or highly conserved across species from yeast to humans (Supplementary information, Figs. S4c, d, S6). The well-accepted highly conserved catalytic mechanism suggests that human Pol III in elongation state unwinds the downstream double-stranded DNA in the active center region, where the transcribed RNA forms a hybrid with template strand.

Despite the generally similar architecture shared by human and yeast Pol III, the human Pol III structure reveals that Pol III-specific RPC3–RPC6–RPC7 heterotrimer and RPC10 adopt conformations distinct from their counterparts in yeast Pol III structures (Figs. 2–4).

The human Pol III-specific heterotrimer RPC3–RPC6–RPC7

The RPC3–RPC6–RPC7 heterotrimer packs against the clamp, seals the active cleft, and connects to the stalk (RPC8–RPC9) (Figs. 2b, 3a; Supplementary information, Movie S3). RPC3 adopts a rigid fold, in which the C-terminal coiled-coil (CC) inserts into the central hole formed by four preceding winged helix (WH1–WH4) domains, consistent with a previously published crystal structure of RPC3.[16] The extensively packed WH domains and the CC of RPC3 together nucleate heterotrimer assembly (Fig. 2b). RPC6 has three predicted winged helix domains (WH1–WH3) followed by an iron-sulfur domain.[36] Relatively weak cryo-EM map shows that WH1 and WH2 domains of RPC6 are suspended above the nucleic acid-binding cleft but leave the DNA exit tunnel open (Figs. 1b, c, 3a–c; Supplementary information, Fig. S9a). The architectural positioning of WH1 and WH2 domains was further confirmed by crosslinking mass spectrometry, which reveals a number of crosslinks between residues of WH1 or WH2 of RPC6 and their surrounding residues of RPC2 and RPC3 (Supplementary information, Fig. S10). The WH3 of RPC6 interacts with the WH3 and WH4 of RPC3 and the iron-sulfur domain packs against the helix pair (α17, α20) and WH4 of RPC3 (Fig. 2b, h). The RPC7 subunit winds on the surface of RPC3–RPC6 (Fig. 2b, h, i). The overall fold of RPC3 and the clamp–RPC3 contacts are generally similar to those in yeast Pol III EC structure.[30] However, RPC6 and RPC7 are largely distinct from their counterparts in yeast, consistent with their functions supporting elaborate regulation in mammalian system (described below).

RPC7 binds Pol III stalk and clamp

The RPC7 subunit threads through the RPC3–RPC6 and interacts with the clamp of Pol III core module and the stalk module (Fig. 2b, g, i). From the N-terminus to the C-terminus, RPC7 binds the parallel helices of the clamp at the edge of DNA exit tunnel, spans over the iron-sulfur domain of RPC6, packs on a V-shaped groove formed by the CC and WH1–WH2 of RPC3, forms a helix hairpin that interacts with the stalk on a shallow groove formed by RPC8, RPC9 and RPC1, and folds back and winds over the other surfaces of WH1 and WH2 of RPC3 (Fig. 2b, g, i). This conformation largely differs from that of yeast Pol III EC[30] and reveals structural features of human Pol III.

A characteristic structural feature of human Pol III is that the heterotrimer module and the stalk module are bridged by a helix

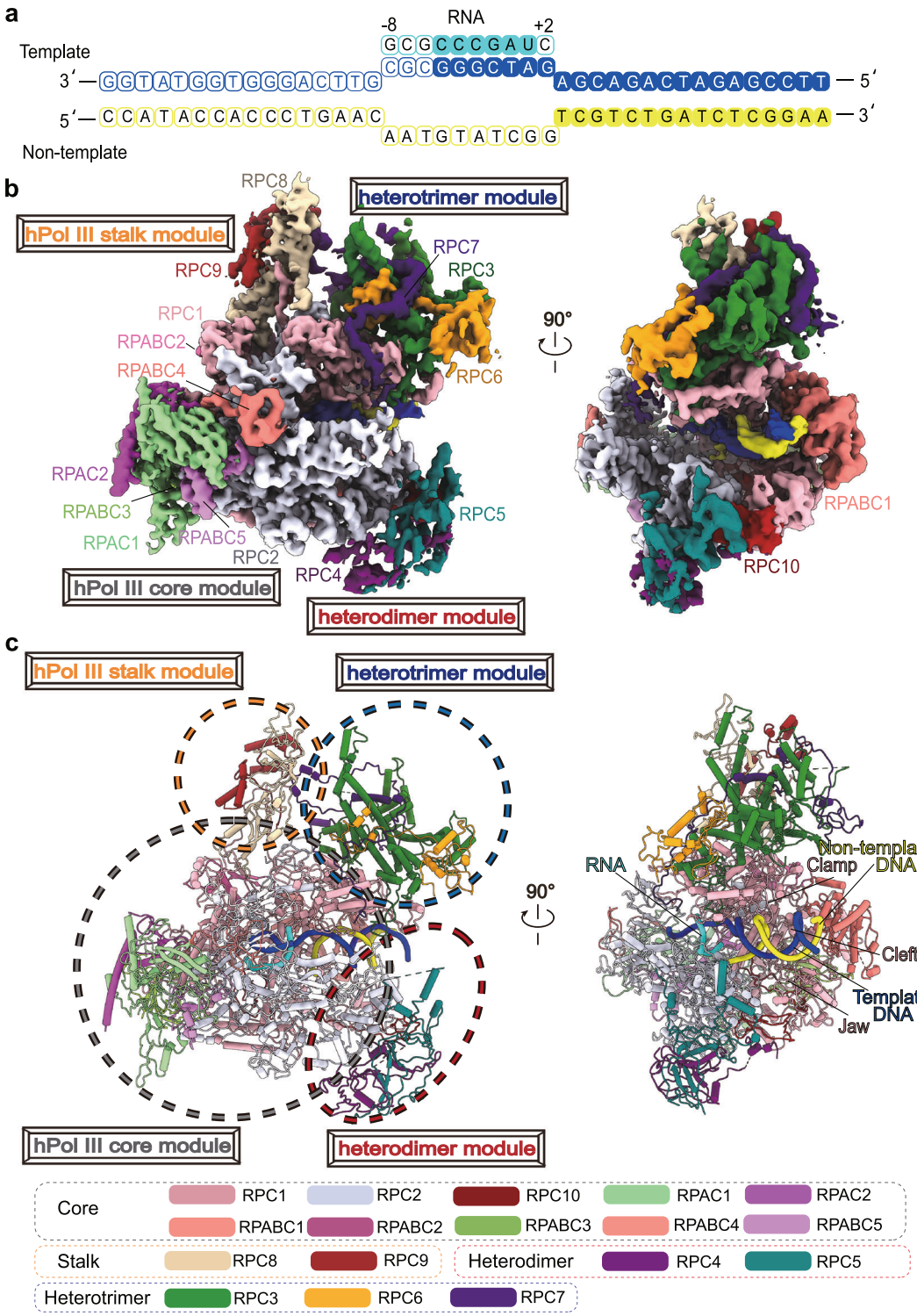

Fig. 1 Cryo-EM structure of the human Pol III EC. a Schematic model of the transcription scaffold used in this study. The template DNA is shown in blue, the non-template DNA in yellow, and RNA in cyan. RNA is numbered relative to the transcription start site in the elongation complex. Mismatched bases depict the mimetic transcription bubble. The bases that built in our model are shown with color-filled circles. **b** Cryo-EM maps of human Pol III EC in two different views. The positions of Pol III subunits are labeled. **c** Cartoon representation of Pol III EC structure. Four modules are highlighted with dashed circles. Color scheme is shown below the figure and used in all figures.

hairpin of RPC7 (RPC7 Met68–Try95) (Fig. 2i). This bridge is the sole connection between the heterotrimer and the stalk and is absent in the previously reported yeast Pol III structure,[30] suggesting an acquired structural feature in humans or other higher eukaryotes during evolution. Since the heterotrimer RPC3–RPC6–RPC7 plays a role in Pol III transcription initiation complex formation, this helix hairpin may provide stable connection for the heterotrimer to the rest of the enzyme and facilitate transcription.

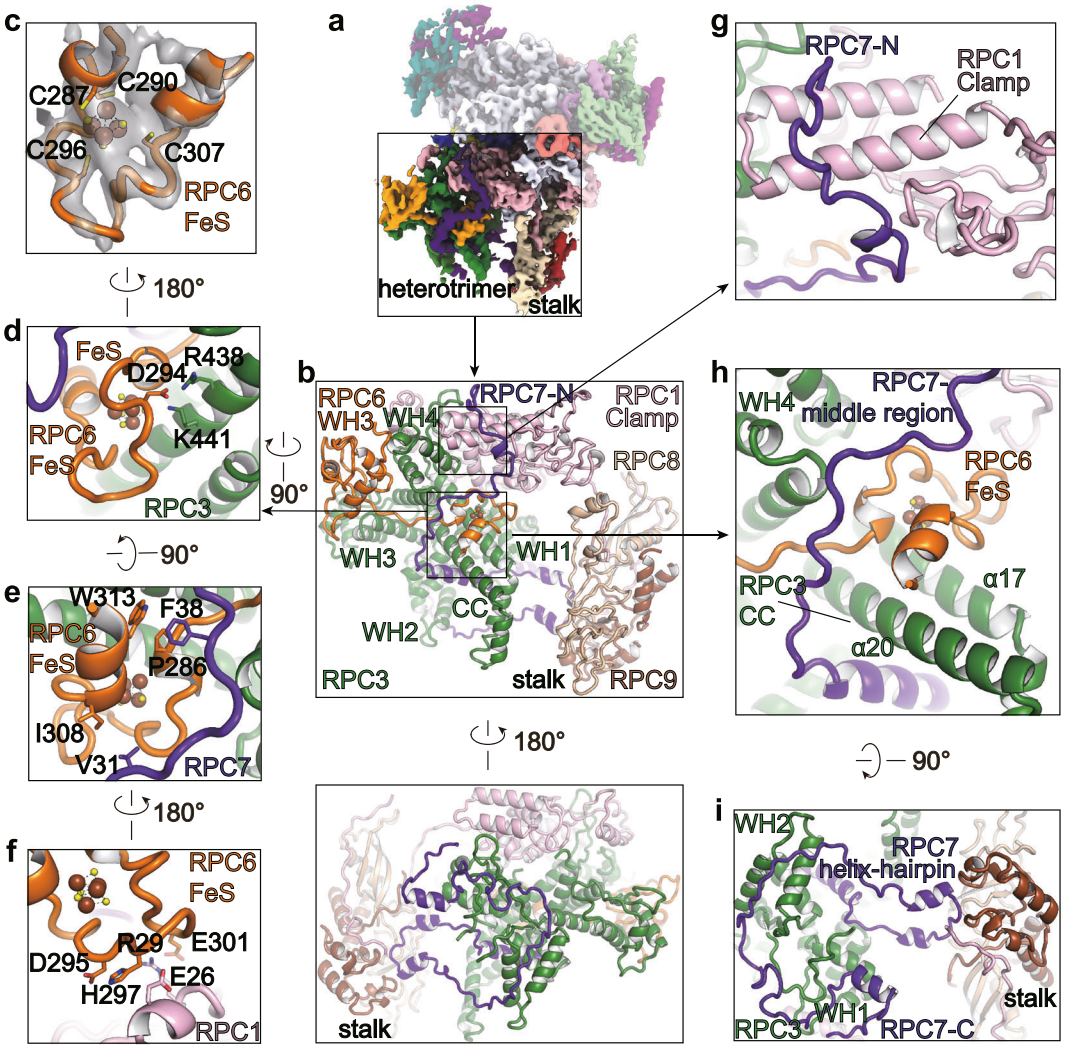

Fig. 2 Structural organization of the RPC3–RPC6–RPC7 heterotrimer. a Cryo-EM map of the Pol III EC with the heterotrimer and stalk modules highlighted. **b** Close-up views of structural organization of subunits RPC3, RPC6 and RPC7. WH winged helix, CC coiled coil. **c** Close-up view of structural model and cryo-EM density of FeS cluster. **d–f** Intermolecular interactions mediated by the FeS cluster of RPC6. Residues involved in the interactions are shown in stick representation. **g–i** Close-up views of contacts between RPC7 and RPC1 (**g**), RPC6 (**h**), RPC3 (**h**, **i**), and the stalk (**i**), respectively.

The RPC6 FeS domain mediates heterotrimer–core contacts

It has been known that human RPC6 contains a C-terminal cubane [4Fe-4S] cluster.[36] The cryo-EM map reveals outstanding density of iron-sulfur cluster even at high threshold, showing much stronger density than its surrounding regions. The iron-sulfur cluster adopts a characteristic FeS fold through coordination with four cysteine residues (C287, C290, C296, C307) at the C-terminus of RPC6 (Fig. 2c). The FeS domain of RPC6 establishes multiple interactions with the heterotrimer subunits RPC3 and RPC7 and the core subunit RPC1. Residue D294 of RPC6 forms hydrogen bonds with residues K441 and R438 of RPC3 (Fig. 2d). Residues W313, I308 and P286 make hydrophobic contacts with residues F38 and V31 of RPC7 (Fig. 2e). Residues D295, E301, and H297 of RPC6 establish a network of hydrogen bonds with residues E26 and R29 of RPC1 (Fig. 2f). Therefore, the FeS domain of RPC6 serves as a molecular guide that leads the N-terminal loop of RPC7 toward the clamp and the DNA exit tunnel. Consistent with the observed structural role of C-terminal FeS domain in mediating contacts between Pol III core and the RPC3–PRC6–RPC7 trimer, the C-terminal mutation of yeast C34 (human RPC6) leads to dissociation of the trimer from Pol III and abolishes the elongation activity.[37] Nevertheless, the presence of FeS cluster domain in RPC6 suggests a role in stabilizing human Pol III. Intriguingly, FeS domain does not exist in yeast RPC6, in which the equivalent region forms an extended loop but lacks the four equivalent cysteine residues (Supplementary information, Fig. S8a).[30] The FeS domain in human Pol III and the equivalent region in yeast Pol III are placed in a similar position, suggesting a conserved function.

The WH1 and WH2 domains of RPC6 seal the DNA-binding cleft

The cryo-EM map shows that the N-terminal WH1 domain of RPC6 is suspended above the DNA-binding cleft and bridges the RPC1 clamp and the RPC2 protrusion and lobe (Fig. 3a; Supplementary information, Fig. S9a and Movie S3). The WH1 and WH2 of RPC6 make contacts with RPC4–RPC5 but do not directly bind DNA. The interaction between WH1 and the N-terminal tail of RPC7α results in a more closed cleft compared to that of yeast Pol III EC (PDB:5FJ8).[30] The positioning of WH1 is likely stabilized by the N-terminal tail of RPC7α (described below). Interestingly, a WH domain-mediated cleft sealing was observed in yeast Pol I EC,[38] in which the C-terminal tandem winged helix (tWH) domain of A49 (equivalent to RPC5 in Pol III) binds upstream DNA and is proposed to enhance Pol I processivity. Although the clefts of Pol I and Pol III are sealed by WH domains of distinct subunits in

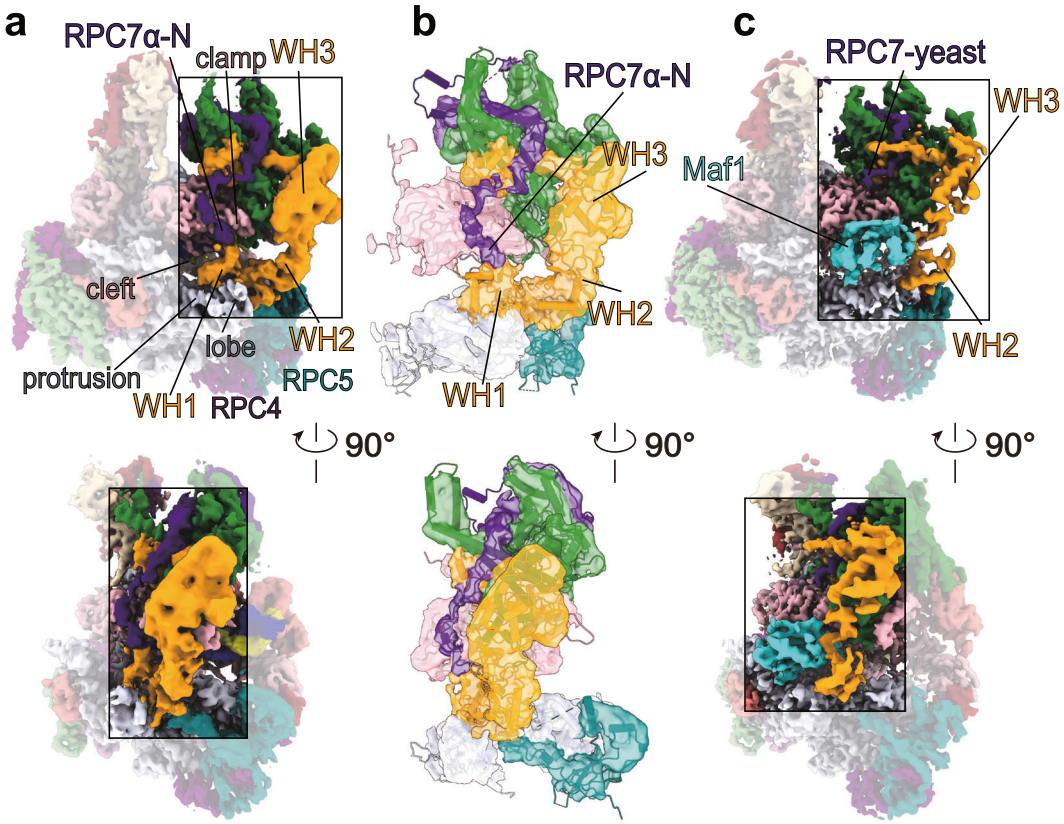

Fig. 3 RPC7α binds the WH1 domain of RPC6 and prevents Maf1 binding. a A combined cryo-EM map of human Pol III EC shown in two different views. The localizations of RPC6 (yellow) and RPC7 (blue) are highlighted. **b** Locally refined cryo-EM map around the WH1 and WH2 domains of RPC6 is shown in transparent surface with the structural model of Pol III and the predicted model of RPC6 WH1 shown in cartoon. **c** Cryo-EM map of yeast Pol III–Maf1 complex shown as in **a**, **b**. Density of RPC6 (yellow), RPC7 (blue) and Maf1 (cyan) are highlighted.

distinct manners, the shared cleft sealing may favor the formation of a stable transcription elongation complex.

RPC6 and RPC7α prevent Maf1-mediated inhibition of transcription

In vitro biochemical studies demonstrated that Maf1 binds Pol III and prevents PIC formation in both yeast and human cells.[25,39] Direct Maf1–Brf1 interaction was confirmed and the interaction was shown to inhibit the recruitment of Brf1 to TFIIIC–DNA complexes.[25,40,41] Recently reported cryo-EM structure of yeast Maf1–Pol III complex illustrated that Maf1 binds Pol III between the RPC2 protrusion, the clamp CC helices, and the WH2 of RPC6.[26] Aromatic stacking between invariable W319 of Maf1 and W294 of C160 (yeast counterpart of human RPC1) may stabilize their binding. Comparison of human Pol III EC structure and yeast Pol III–Maf1 structure reveals that Maf1 may clash with upstream DNA and block the DNA exit tunnel, consistent with the finding in yeast system (Supplementary information, Fig. S5). This may explain why Maf1 can repress the transcription activity on longer upstream DNA rather than shorter upstream DNA.[42]

Structural comparison of human Pol III and yeast Pol III–Maf1 complex also shows that Maf1 binding would introduce steric hindrance with the WH1 of RPC6 and the N-terminal region of RPC7α, suggesting a competitive binding of Pol III core around the DNA exit tunnel (Fig. 3b, c). The binding of RPC6–RPC7α is evident, suggesting a regulatory role of these domains in preventing Maf1-mediated inhibition of Pol III activity. This could explain why the Pol III activity is upregulated in tumor cells where RPC7α is the dominant isoform in Pol III.[28] This is in line with the fact that the WH1 of RPC6 in our structure is positioned differently from that in the yeast Pol III PIC structure (PDB: 6F40) (Supplementary information, Fig. S4e, f) and is missing in the yeast Pol III–Maf1 structure (PDB: 6TUT) (Fig. 3c).

TFIIS-like RPC10 is positioned near the active site of Pol III in the backtracked state

RPC10 consists of an N-terminal RPB9-like zinc ribbon (N-ribbon) and a C-terminal TFIIS-like zinc ribbon (C-ribbon) (Fig. 4a, b). Similar to C11 (counterpart of RPC10) of yeast Pol III[30] and RPB9 of the Pol II,[43,44] the N-ribbon of RPC10 inserts into a pocket formed by the lobe of RPC2, the jaw of RPC1, and TFIIF-like RPC4–RPC5 heterodimer (Fig. 4c). The linker connecting the two ribbons packs against the RPC1 jaw (Fig. 4d). The C-ribbon in the backtracked state inserts into the polymerase funnel formed by the active cleft, the funnel helices, and the pore (Fig. 4d). In contrast, the C-ribbon is more flexible in Pol III in the post-translocation state (Fig. 4a, right panel; Supplementary information, Fig. S2l), consistent with its lack of stable positioning during forward elongation.

The cryo-EM map of Pol III in the backtracked state shows that the C-ribbon points toward the growing 3′ end of RNA and is ~18 Å away from the first modeled RNA phosphate group, indicating the lack of direct contact with RNA end, consistent with relatively weak cryo-EM density around the C-ribbon (Fig. 4d). The structural observation is consistent with the known RNA cleavage activity of the yeast C11 and its essential role in efficient transcription termination.[24] The architectural placement of the RPC10 C-ribbon suggests that RPC10 is involved in transcription termination probably through a mechanism similar to TFIIS-mediated RNA cleavage in Pol II proofreading and arrest.[45,46] It has been known that both yeast C11 (human RPC10) and C53–C37 (human

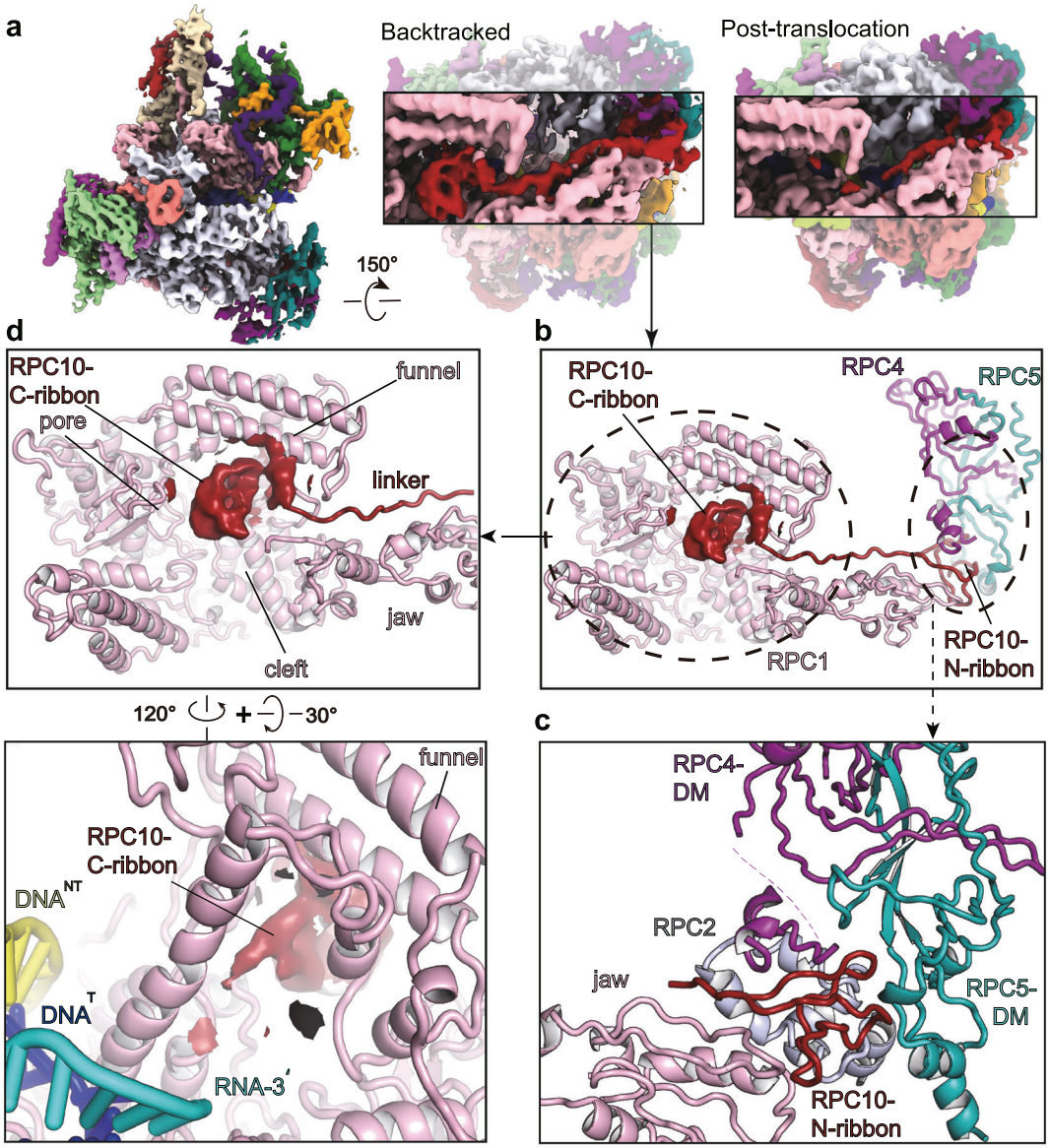

Fig. 4 TFIIS-like subunit RPC10 in Pol III EC. a Cryo-EM map of human Pol III EC with close-up views of RPC10 in the backtracked and post-translocation states shown. The map of RPC10 (red) is highlighted. **b** Close-up view of structural model of RPC10 N-ribbon and density map of RPC10 C-ribbon and contacting regions that are indicated with dashed circles. **c** Close-up view of structural model of RPC10 N-ribbon and its interaction with subunits RPC4, RPC5, RPC1 and RPC2. **d** Close-up view of structural model of the linker and density map of C-ribbon of RPC10 and binding regions of subunit RPC1. Two different views are shown. The density shows that the RPC10 C-ribbon points toward the RNA 3′ end.

RPC4–RPC5) dimer are required for Pol III transcription termination at a tract of thymidines.[17,21] RPC4–RPC5 may provide a dock to anchor the N-ribbon of RPC10 to Pol III. Nevertheless, our Pol III structure provides a basis for understanding the functional connection between the N-ribbon-associated RPC4–RPC5 dimer and the C-ribbon-associated active center.

Potential effects of disease-associated Pol III mutations

Mutations of Pol III subunits have been reported to be associated with human diseases, such as Treacher Collins syndrome (TCS),[10] Wiedemann-Rautenstrauch syndrome (WRS),[47] hypomyelinating leukodystrophy (HLD),[48,49] and susceptibility to varicella zoster virus.[50,51] We mapped disease-causative mutations on human Pol III structure and found that some mutations are localized at the intermolecular interface of the core module and possibly impair the complex integrity or enzymatic activity (Fig. 5a). For example, mutation of L51 to arginine (L51R) of RPAC2 in TCS is likely to disrupt the hydrophobic contact at RPAC1–RPAC2 interface and mutation R56C likely causes loss of contact with residue E996 of RPC2 (Fig. 5b). In WRS, mutations G903R and D1292N of RPC1 may cause instability of RPC1 (Fig. 5c). In HLD, mutations T26I and N32I of RPAC1 may disrupt its interaction with RPAC2, RPABC3, RPC1 and RPC2 (Fig. 5d), and mutation E1261K of RPC1 may disrupt the interaction between RPC1 and RPABC1 (Fig. 5e). In susceptibility to varicella zoster virus, mutation R582C of RPC1 may lead to loss of contacts with residue E74 of RPABC3 (Fig. 5f), and mutation R438G of RPC3 may disrupt its interaction with residues D294 and D295 of RPC6 (Fig. 5g). High-resolution structure of human Pol III serves as a scaffold to further investigate the structural-functional relationship of other disease-associated mutations.

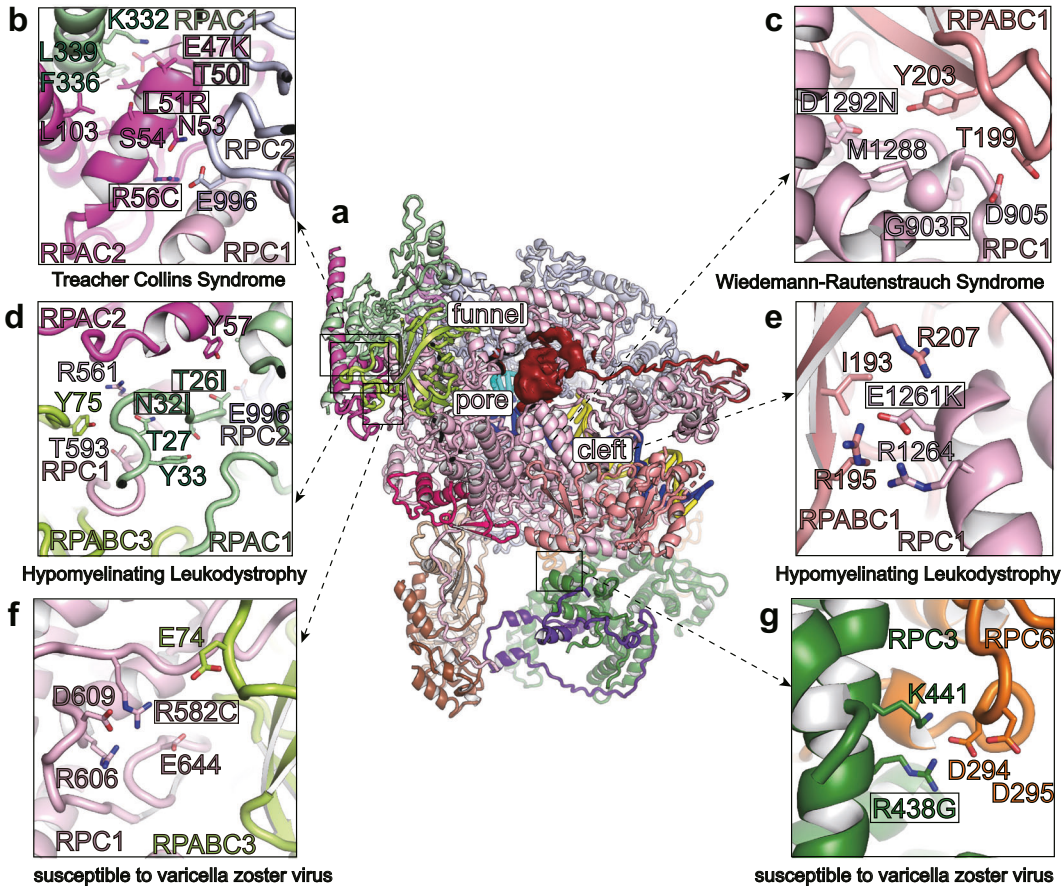

Fig. 5 Disease-associated mutations in human Pol III. a Overall view of human Pol III structure. **b**–**g** Representative disease-associated mutations of Pol III in Treacher Collins Syndrome (**b**), Wiedemann-Rautenstrauch Syndrome (**c**), Hypomyelinating Leukodystrophy (**d**, **e**), and susceptibility to varicella zoster virus (**f**, **g**) are shown in close-up views. Mutations are highlighted with dark boxes and their binding residues are shown in stick representation.

DISCUSSION

In this study, we reconstituted human Pol III EC and determined the cryo-EM structures of Pol III in the backtracked and post-translocation states, respectively. The Pol III EC structures at near-atomic resolution reveal catalytic core module similar to that of yeast Pol III EC. The structures also reveal details of the human Pol III-specific TFIIE-like heterotrimeric subcomplex RPC3–RPC6–RPC7, the TFIIS-like core subunit RPC10, and RPC7α conferring resistance to Maf1-mediated repression, which were not observed in yeast Pol III structures.[26,30,31,33]

It has been known that dysregulation of Pol III is associated with a variety of human diseases and Maf1 is a critical repressor of Pol III.[12] Intriguingly, no direct association between Maf1 and human disease has been reported. Our structure shows that the N-terminal region of RPC7α contacts the WH1 domain of RPC6 and would prevent Maf1 interaction with Pol III, indicating that Pol IIIα (RPC7α-containing Pol III) possesses high transcription activity due, at least in part, to the lack of Maf1-mediated repression. As RPC7 is the only subunit that has two isoforms in mammalian Pol III, the N-terminal region of two isoforms of RPC7 could be a key Pol III regulatory element that confers distinct transcriptional responses to the Maf1-mediated repression.

It has been shown that Maf1 overlaps with TFIIIB in Pol III PIC and inhibits transcription initiation.[26] Comparison of our human Pol III EC structure and yeast Pol III–Maf1 structure suggests that Maf1 might also directly block the exit tunnel of upstream DNA and therefore repress Pol III transcription. As Pol III transcription products are essential for protein synthesis and cell growth, it is reasonable that cells may use redundant mechanisms to ensure that the Pol III activity is under tight control. Further experiments are required to investigate potential inhibitory role of Maf1 in Pol III-mediated transcription beyond the assembly of PIC.

The iron-sulfur cluster at RPC6 C-terminal region was assigned in the cryo-EM map. Our structure reveals that the iron-sulfur cluster of RPC6 stabilizes the assembly of heterotrimer by establishing an interaction network with other two subunits RPC3 and RPC7. For example, the [4Fe-4S] cluster of the TFEα/β in archaea, an evolutionary ancestor of TFIIE-like RPC3/RPC6, is essential for heterodimerization and engagement with the RNAP clamp.[36] It has been known that the iron-sulfur cluster can be used as a sensor for cells to respond to oxidative stress and subsequently regulate gene expression.[52] Therefore, it is tempting to speculate that the iron-sulfur cluster of RPC6 may provide another layer of regulation for Pol III transcription.

In summary, our structures reveal that the FeS cluster, the WH1 domain of RPC6 and the N-terminal region of RPC7 are regulatory elements for human Pol III transcription. Our study also reveals a fundamental mechanism of regulation of Pol III transcription activity by Maf1 and RPC7α.

MATERIALS AND METHODS

Protein expression and purification

The ORFs of 17 subunits of human Pol III (with RPC7α included) were individually subcloned into a modified pCAG vector. RPC2 is N-terminally Protein A tagged and all the rest of subunits are untagged. The expression cassettes of 17 subunits were merged into 6 plasmids, in particular, RPC1 and RPC2 were in the first and

second plasmids, RPC3/RPC4/RPC5 were merged as the third plasmid, RPC6/RPABC3/RPABC4/RPABC5 were merged as the fourth plasmid, RPC7/RPC8/RPC9/RPC10 were merged as the fifth plasmid, and RPAC1/RPAC2/RPABC1/RPABC2 were merged as the sixth plasmid. Each ORF was driven by a CAG promoter. The six plasmids were co-transfected into HEK Expi293 cells using PEI. After being cultured at 37 °C for 48 h, cells were harvested and lysed for 30 min in buffer containing 20 mM HEPES (pH 8.2), 200 mM NaCl, 0.25% CHAPS, 10 μM $ZnCl_2$, 5 mM ATP, 5 mM $MgCl_2$, 10% glycerol and 2 mM DTT supplemented with 1 mM PMSF, 1 μg/mL Aprotinin, 1 μg/mL Pepstatin, 1 μg/mL Leupeptin at 4 °C. The lysate was centrifuged at 15,000× *g* for 30 min at 4 °C. The supernatant was incubated with IgG beads (Shanghai Raygene Biotechnology Co., equilibrated with lysis buffer before use) for 3 h, and beads was washed five times (20 mL each) with buffer containing 20 mM HEPES (pH 8.2), 200 mM NaCl, 0.05% CHAPS, 10% glycerol, 5 mM ATP, 5 mM $MgCl_2$, 10 μM $ZnCl_2$ and 2 mM DTT. The tags were removed by on-column cleavage overnight followed by elution with a buffer containing 20 mM HEPES (pH 8.2), 150 mM NaCl, 0.05% CHAPS, 10% glycerol, 2 mM $MgCl_2$, 10 μM $ZnCl_2$ and 2 mM DTT. The eluted protein was further purified using an anion exchange column (mono Q) in HEPES (pH 8.2) buffer with increasing concentrations of NaCl from 150 to 1000 mM. The Pol III complex was eluted when NaCl concentration reached 400 mM, followed by dialysis against low salt buffer (similar to mono Q buffer but containing 150 mM NaCl) overnight. The complex was concentrated to ~1.8 mg/mL, then flash-frozen in liquid nitrogen and stored at −80 °C.

Scaffold preparation

For the preparation of elongation complexes, 42-nt long DNA scaffolds based on human 5S rRNA gene were used. The sequence contains the 5S rRNA gene promoter from +9 to +50, for the DNA–RNA hybrid in the backtracked state, a 10-nt mismatch from +25 to +34 (template strand: 5′-TTCCGAGATCAGACGA GATCGGGCGCGTTCAGGGTGGTATGG-3′, non-template strand: 5′-CCATACCACCCTGAACAATGTATCGGTCGTCTGATCTCGGAA-3′, RNA 5′-GCGCCCGAUC-3′), and for the post-translocation state, a 10-nt mismatch from +23 to +32 (template strand: 5′-TTCCGAGA TCAGACGAGATCGGGCTTTCTCAGGGTGGTATGG-3′, non-template strand: 5′-CCATACCACCCTGAGAAATGTATCGGAAGTCTGATCTCG-GAA-3′, RNA 5′-GCGCCCGAUC-3′). The oligonucleotides were suspended in DEPC H_2O to a final concentration of ~5 μM, mixed in equimolar concentration and heated to 95 °C for 10 min. The reaction was cooled to 20 °C at a rate of 1 °C per min. To obtain DNA–RNA hybrid, DNA duplex was incubated with a 1.2-fold excess of RNA for 10 min at 40 °C and then cooled to 4 °C.

EC assembly

For in vitro reconstitution of the Pol III EC, 20 μL of 1.8 mg/mL Pol III was incubated with a 2-fold excess of DNA–RNA scaffold for 30 min on ice. Sample was dialyzed against buffer (20 mM HEPES, pH 8.0, 150 mM NaCl, 2 mM $MgCl_2$, 2 mM DTT) at 4 °C using Slide-a-lyzer mini dialysis pins (10,000 MW cut-off, Thermo Fisher).

Cryo-EM sample preparation

For negative staining EM grid preparation, 5 μL of Pol III EC sample were applied onto glow-discharged copper grids supported by a continuous thin layer of carbon film for 60 s before negative staining by 2% (w/v) uranyl formate solution at room temperature. The grids were prepared in the Ar/O_2 mixture for 15 s using a Gatan 950 Solarus plasma cleaning system with a power of 35 W. The negatively stained grids were loaded onto a Thermo Fisher Scientific Talos L120C microscope equipped with a Ceta CCD camera and operated at 120 kV at a nominal magnification of 92,000×, corresponding to a pixel size of 1.58 Å on the specimen.

For cryo-EM grid preparation, 4 μL of the sample at a concentration of ~0.5 mg/mL Pol III EC were applied to freshly glow-discharged Quantifoil R1.2/1.3 holey carbon grids. After incubation for 5 s at 4 °C and 100% humidity, the grids were blotted for 2–3 s in a Thermo Fisher Scientific Vitrobot Mark IV and plunge-frozen in liquid ethane at liquid nitrogen temperature. The grids were prepared in the H_2/O_2 mixture for 60 s using a Gatan 950 Solarus plasma cleaning system with a power of 5 W. The ø 55/20 mm blotting paper is made by TED PELLA used for plunge freezing.

Data collection

The cryo-EM grids of Pol III EC were loaded onto a Thermo Fisher Scientific Titan Krios transmission electron microscope operated at 300 kV for data collection. The dataset 1 (backtracked state) cryo-EM images were automatically recorded by a Gatan K3 Summit direct electron detector in the super-resolution counting mode using Serial-EM[53] with a nominal magnification of 22,500× in the TEM mode, which yielded a super-resolution pixel size of 0.53 Å on the image plane, and with defocus values ranging from 1.0 to 2.5 μm. Each micrograph stack was dose-fractionated to 40 frames with a total electron dose of ~50 $e^-/Å^2$ and a total exposure time of 3.2 s. 4700 micrographs were collected for further processing.

The dataset 2 (post-translocation state) cryo-EM images were automatically recorded by a post-GIF Gatan K2 Summit direct electron detector in the super-resolution counting mode using Serial-EM[53] with a nominal magnification of 130,000× in the EFTEM mode, which yielded a super-resolution pixel size of 0.522 Å on the image plane, and with defocus values ranging from 1.0 to 2.5 μm. Each micrograph stack was dose-fractionated to 32 frames with a total electron dose of ~50 $e^-/Å^2$ and a total exposure time of 6.8 s. 6500 micrographs were collected for further processing.

Image processing

For cryo-EM dataset 1, drift and beam-induced motion correction were applied on the super-resolution movie stacks using MotionCor2[54] and binned 2-fold to a calibrated pixel size of 1.06 Å/pix. The defocus values were estimated by Gctf[55] from summed images without dose weighting. Other procedures of cryo-EM data processing were performed within RELION v3.0[56,57] and cryoSPARC v2[56,57] using the dose-weighted micrographs.

2,377,755 particles were picked by automatic particle picking in RELION without reference and subjected to reference-free 2D classification. 1,062,406 particles were selected from good 2D classes for 3D classification in RELION. 320,170 particles were selected from good 3D classes, which were used for homogeneous refinement in cryoSPARC and CTF refinement, yielding a reconstruction of Pol III EC (backtracked state) at 3.0 Å resolution.

320,170 particles were subjected to Local search 3D classification with 1.8 degree. 98,293 particles were selected from good 3D class, which were used for homogeneous refinement in cryoSPARC and CTF refinement, yielding an Insert Funnel conformation of the Pol III EC at 3.5 Å resolution.

320,170 particles were subjected to 3D classification with mask at RPC6 WH2 and WH1 domains. 67,080 particles were selected from good 3D class, which were used for refinement in RELION, yielding a masked RPC6 WH2 and WH1 domains of the Pol III EC at 4.1 Å resolution.

For cryo-EM dataset 2, drift and beam-induced motion correction were applied on the super-resolution movie stacks using MotionCor2[54] and binned 2-fold to a calibrated pixel size of 1.044 Å/pix. The defocus values were estimated by Gctf[55] from summed images without dose weighting. Other procedures of cryo-EM data processing were performed within RELION v3.0 [56,57] and cryoSPARC v2[56,57] using the dose-weighted micrographs.

1,107,487 particles were picked by automatic particle picking in RELION without reference and subjected to reference-free 2D classification. 563,769 particles were selected from good 2D classes for heterogeneous refinement in cryoSPARC. 64,111 particles were selected from good 3D classes, which were used

for homogeneous refinement in cryoSPARC and CTF refinement, yielding a reconstruction of Pol III EC (post-translocation state) at 3.35 Å resolution.

All reported resolutions are based on the gold-standard Fourier shell correlation (FSC) = 0.143 criterion. The GSFSC curves were corrected for the effects of a soft mask with high-resolution noise substitution. All cryo-EM maps were sharpened by applying a negative B-factor estimation in cryoSPARC Sharpening Tools. All the visualization and evaluation of the 3D volume map were performed within UCSF Chimera or UCSF ChimeraX,[58] and the local resolution variations were calculated using cryoSPARC.

Model building and structure refinement

The cryo-EM maps of the Pol III EC in the backtracked and post-translocation states were used for model fitting, respectively. The structures of yeast Pol III EC (PDB: 5FJ8)[30] was used as initial structural templates, which were docked into the cryo-EM maps by rigid-body fitting using UCSF Chimera.[58] The structural models of WH1 and WH2 domains of RPC6 were predicted based on sequences using phyre2[59] and docked into the cryo-EM map associated with RPC6 WH3 domain for structural analysis (shown in figures and movies) but were not built in structural model due to the relatively weak cryo-EM map. The two structural models were built in COOT[60] and refined in real space using Phenix[61] with secondary structure and geometry restraints using the cryo-EM map of the Pol III EC. Disordered regions that could not be built in each subunit are listed in Supplementary information, Table S2. Overfitting of the model was monitored by refining the model in one of the two half maps from the gold-standard refinement approach and testing the refined model against the other map.[62] Statistics of the map reconstruction and model refinement can be found in Supplementary information, Table S1. The final models were evaluated using MolProbity.[63] Map and model representations in the figures and movies were prepared by PyMOL (https://pymol.org/),[64] UCSF Chimera or UCSF ChimeraX.[65]

Crosslinking mass spectrometry

The Pol III EC (0.75 μg/μL) was crosslinked with disuccinimidyl suberate (DSS) in a 1:500 molar ratio at room temperature for 1 h. The reaction was quenched by adding 20 mM ammonium bicarbonate. Crosslinked sample was digested with trypsin overnight. After being quenched by 5% formic acid, the tryptic peptides were desalted with Pierce C18 spin column and separated in a proxeon EASY-nLC liquid chromatography system by applying a step-wise gradient of 0%–85% acetonitrile in 0.1% formic acid. Peptides eluted from the liquid chromatography column were directly electrosprayed into the mass spectrometer with a distal 2 kV spray voltage. Data-dependent tandem mass spectrometry (MS/MS) analysis was performed on Thermo Q-Exactive instrument in a 60-min gradient. Raw data was processed with pLink software.[66]

DATA AVAILABILITY

The cryo-EM maps have been deposited in the EM Databank under accession numbers: EMD-30779 (backtracked state) and EMDB-30865 (post-translocation state). Atomic coordinates have been deposited in the Protein Data Bank with PDB IDs: 7DN3 (backtracked state) and 7DU2 (post-translocation state).

ACKNOWLEDGEMENTS

We thank Center of Cryo-Electron Microscopy of Fudan University, Center of Cryo-Electron Microscopy of ShanghaiTec University, Center for Biological Imaging of Institute of Biophysics of Chinese Academy of Sciences, and National Center for Protein Science Shanghai for support in cryo-EM data collection and data analyses, and the Biomedical Core Facility of Fudan University for support in mass spectrometry analyses. This work was supported by the National Key R&D Program of China (2016YFA0500700), the National Natural Science Foundation of China (32030055, 31830107, 31821002), the Shanghai Municipal Science and Technology Major Project (2017SHZDZX01), Shanghai Municipal Science and Technology Commission (19JC1411500), the Science and Technology Major Project of Inner Mongolia Autonomous Region of China to the State Key Laboratory of Reproductive Regulation and Breeding of Grassland Livestock, the National Ten-Thousand Talent Program (Y.X.), the National Program for support of Top-Notch Young Professionals (Y.X.), and the Strategic Priority Research Program of the Chinese Academy of Sciences (XDB08000000).

AUTHOR CONTRIBUTIONS

Y.X. supervised the project. L.L., H.H., Z.Y. and Y.X. designed the experiments. D.Z. collected ORFs of 17 subunits of Pol III. L.L. did subcloning and purified the proteins. H.H. designed nucleic acid scaffold and assembled EC complex. Y.R. helped checking negative staining samples. Z.Y. prepared the cryo-EM samples, collected the data and determined the structures. L.L. and Z.Y. built the structural models. L.L., Z.Y., H.H., and Y.X. analyzed the data and wrote the manuscript.

ADDITIONAL INFORMATION

Supplementary information The online version contains supplementary material available at https://doi.org/10.1038/s41422-021-00472-2.

Competing interests: The authors declare no competing interests.

REFERENCES

1. Cramer, P. et al. Structure of eukaryotic RNA polymerases. *Annu. Rev. Biophys.* **37**, 337–352 (2008).
2. Roeder, R. G. & Rutter, W. J. Multiple forms of DNA-dependent RNA polymerase in eukaryotic organisms. *Nature* **224**, 234–237 (1969).
3. Vannini, A. & Cramer, P. Conservation between the RNA polymerase I, II, and III transcription initiation machineries. *Mol. Cell* **45**, 439–446 (2012).
4. White, R. J. Transcription by RNA polymerase III: more complex than we thought. *Nat. Rev. Genet.* **12**, 459–463 (2011).
5. Dieci, G., Fiorino, G., Castelnuovo, M., Teichmann, M. & Pagano, A. The expanding RNA polymerase III transcriptome. *Trends Genet.* **23**, 614–622 (2007).
6. Dieci, G. & Sentenac, A. Facilitated recycling pathway for RNA polymerase III. *Cell* **84**, 245–252 (1996).
7. Arimbasseri, A. G., Rijal, K. & Maraia, R. J. Transcription termination by the eukaryotic RNA polymerase III. *Biochim. Biophys. Acta* **1829**, 318–330 (2013).
8. White, R. J. RNA polymerases I and III, non-coding RNAs and cancer. *Trends Genet.* **24**, 622–629 (2008).
9. Goodarzi, H. et al. Modulated expression of specific tRNAs drives gene expression and cancer progression. *Cell* **165**, 1416–1427 (2016).
10. Dauwerse, J. G. et al. Mutations in genes encoding subunits of RNA polymerases I and III cause Treacher Collins syndrome. *Nat. Genet.* **43**, 20–22 (2011).
11. Thiffault, I. et al. Recessive mutations in POLR1C cause a leukodystrophy by impairing biogenesis of RNA polymerase III. *Nat. Commun.* **6**, 7623 (2015).
12. Yeganeh, M. & Hernandez, N. RNA polymerase III transcription as a disease factor. *Genes Dev.* **34**, 865–882 (2020).
13. Wang, Z. & Roeder, R. G. Three human RNA polymerase III-specific subunits form a subcomplex with a selective function in specific transcription initiation. *Genes Dev.* **11**, 1315–1326 (1997).
14. Brun, I., Sentenac, A. & Werner, M. Dual role of the C34 subunit of RNA polymerase III in transcription initiation. *EMBO J.* **16**, 5730–5741 (1997).
15. Kenneth, N. S., Marshall, L. & White, R. J. Recruitment of RNA polymerase III in vivo. *Nucleic Acids Res.* **36**, 3757–3764 (2008).
16. Lefevre, S. et al. Structure-function analysis of hRPC62 provides insights into RNA polymerase III transcription initiation. *Nat. Struct. Mol. Biol.* **18**, 352–358 (2011).
17. Landrieux, E. et al. A subcomplex of RNA polymerase III subunits involved in transcription termination and reinitiation. *EMBO J.* **25**, 118–128 (2006).
18. Kassavetis, G. A., Prakash, P. & Shim, E. The C53/C37 subcomplex of RNA polymerase III lies near the active site and participates in promoter opening. *J. Biol. Chem.* **285**, 2695–2706 (2010).
19. Arimbasseri, A. G. & Maraia, R. J. Mechanism of transcription termination by RNA polymerase III utilizes a non-template strand sequence-specific signal element. *Mol. Cell* **58**, 1124–1132 (2015).
20. Rijal, K. & Maraia, R. J. RNA polymerase III mutants in TFIIFalpha-like C37 that cause terminator readthrough with no decrease in transcription output. *Nucleic Acids Res.* **41**, 139–155 (2013).
21. Mishra, S. & Maraia, R. J. RNA polymerase III subunits C37/53 modulate rU:dA hybrid 3′ end dynamics during transcription termination. *Nucleic Acids Res.* **47**, 310–327 (2019).
22. Iben, J. R. et al. Point mutations in the Rpb9-homologous domain of Rpc11 that impair transcription termination by RNA polymerase III. *Nucleic Acids Res.* **39**, 6100–6113 (2011).

23. Huang, Y., Intine, R. V., Mozlin, A., Hasson, S. & Maraia, R. J. Mutations in the RNA polymerase III subunit Rpc11p that decrease RNA 3′ cleavage activity increase 3′-terminal oligo(U) length and La-dependent tRNA processing. *Mol. Cell. Biol.* **25**, 621–636 (2005).
24. Chedin, S., Riva, M., Schultz, P., Sentenac, A. & Carles, C. The RNA cleavage activity of RNA polymerase III is mediated by an essential TFIIS-like subunit and is important for transcription termination. *Genes Dev.* **12**, 3857–3871 (1998).
25. Desai, N. et al. Two steps in Maf1-dependent repression of transcription by RNA polymerase III. *J. Biol. Chem.* **280**, 6455–6462 (2005).
26. Vorlander, M. K. et al. Structural basis for RNA polymerase III transcription repression by Maf1. *Nat. Struct. Mol. Biol.* **27**, 229–232 (2020).
27. Reina, J. H., Azzouz, T. N. & Hernandez, N. Maf1, a new player in the regulation of human RNA polymerase III transcription. *PLoS ONE* **1**, e134 (2006).
28. Haurie, V. et al. Two isoforms of human RNA polymerase III with specific functions in cell growth and transformation. *Proc. Natl Acad. Sci. USA* **107**, 4176–4181 (2010).
29. Han, Y., Yan, C., Fishbain, S., Ivanov, I. & He, Y. Structural visualization of RNA polymerase III transcription machineries. *Cell Discov.* **4**, 40 (2018).
30. Hoffmann, N. A. et al. Molecular structures of unbound and transcribing RNA polymerase III. *Nature* **528**, 231–236 (2015).
31. Abascal-Palacios, G., Ramsay, E. P., Beuron, F., Morris, E. & Vannini, A. Structural basis of RNA polymerase III transcription initiation. *Nature* **553**, 301–306 (2018).
32. Hoffmann, N. A., Jakobi, A. J., Vorlander, M. K., Sachse, C. & Muller, C. W. Transcribing RNA polymerase III observed by electron cryomicroscopy. *FEBS J.* **283**, 2811–2819 (2016).
33. Vorlander, M. K., Khatter, H., Wetzel, R., Hagen, W. J. H. & Muller, C. W. Molecular mechanism of promoter opening by RNA polymerase III. *Nature* **553**, 295–300 (2018).
34. Cheung, A. C. & Cramer, P. Structural basis of RNA polymerase II backtracking, arrest and reactivation. *Nature* **471**, 249–253 (2011).
35. Wang, D. et al. Structural basis of transcription: backtracked RNA polymerase II at 3.4 angstrom resolution. *Science* **324**, 1203–1206 (2009).
36. Blombach, F. et al. Archaeal TFE alpha/beta is a hybrid of TFIIE and the RNA polymerase III subcomplex hRPC62/39. *Elife* **4**, e08378 (2015).
37. Wei, Y. Y. & Chen, H. T. Functions of the TFIIE-related tandem winged-helix domain of Rpc34 in RNA polymerase III initiation and elongation. *Mol. Cell. Biol.* **38**, e00105–e00117 (2018).
38. Tafur, L. et al. Molecular structures of transcribing RNA polymerase I. *Mol. Cell* **64**, 1135–1143 (2016).
39. Cabart, P., Lee, J. & Willis, I. M. Facilitated recycling protects human RNA polymerase III from repression by Maf1 in vitro. *J. Biol. Chem.* **283**, 36108–36117 (2008).
40. Upadhya, R., Lee, J. & Willis, I. M. Maf1 is an essential mediator of diverse signals that repress RNA polymerase III transcription. *Mol. Cell* **10**, 1489–1494 (2002).
41. Moir, R. D. & Willis, I. M. Regulation of pol III transcription by nutrient and stress signaling pathways. *Biochim. Biophys. Acta* **1829**, 361–375 (2013).
42. Vannini, A. et al. Molecular basis of RNA polymerase III transcription repression by Maf1. *Cell* **143**, 59–70 (2010).
43. Gnatt, A. L., Cramer, P., Fu, J., Bushnell, D. A. & Kornberg, R. D. Structural basis of transcription: an RNA polymerase II elongation complex at 3.3 A resolution. *Science* **292**, 1876–1882 (2001).
44. Cramer, P., Bushnell, D. A. & Kornberg, R. D. Structural basis of transcription: RNA polymerase II at 2.8 angstrom resolution. *Science* **292**, 1863–1876 (2001).
45. Izban, M. G. & Luse, D. S. The RNA polymerase II ternary complex cleaves the nascent transcript in a 3′–5′ direction in the presence of elongation factor SII. *Genes Dev.* **6**, 1342–1356 (1992).
46. Jeon, C. & Agarwal, K. Fidelity of RNA polymerase II transcription controlled by elongation factor TFIIS. *Proc. Natl Acad. Sci. USA* **93**, 13677–13682 (1996).
47. Paolacci, S. et al. Specific combinations of biallelic POLR3A variants cause Wiedemann-Rautenstrauch syndrome. *J. Med. Genet.* **55**, 837–846 (2018).
48. Gauquelin, L. et al. Clinical spectrum of POLR3-related leukodystrophy caused by biallelic POLR1C pathogenic variants. *Neurol. Genet.* **5**, e369 (2019).
49. Daoud, H. et al. Mutations in POLR3A and POLR3B are a major cause of hypomyelinating leukodystrophies with or without dental abnormalities and/or hypogonadotropic hypogonadism. *J. Med. Genet.* **50**, 194–197 (2013).
50. Carter-Timofte, M. E., Hansen, A. F., Christiansen, M., Paludan, S. R. & Mogensen, T. H. Mutations in RNA Polymerase III genes and defective DNA sensing in adults with varicella-zoster virus CNS infection. *Genes. Immun.* **20**, 214–223 (2019).
51. Ogunjimi, B. et al. Inborn errors in RNA polymerase III underlie severe varicella zoster virus infections. *J. Clin. Invest.* **127**, 3543–3556 (2017).
52. Demple, B., Hidalgo, E. & Ding, H. Transcriptional regulation via redox-sensitive iron-sulphur centres in an oxidative stress response. *Biochem. Soc. Symp.* **64**, 119–128 (1999).
53. Mastronarde, D. N. Automated electron microscope tomography using robust prediction of specimen movements. *J. Struct. Biol.* **152**, 36–51 (2005).
54. Zheng, S. Q. et al. MotionCor2: anisotropic correction of beam-induced motion for improved cryo-electron microscopy. *Nat. Methods* **14**, 331–332 (2017).
55. Zhang, K. Gctf: Real-time CTF determination and correction. *J. Struct. Biol.* **193**, 1–12 (2016).
56. Scheres, S. H. RELION: implementation of a Bayesian approach to cryo-EM structure determination. *J. Struct. Biol.* **180**, 519–530 (2012).
57. Kimanius, D., Forsberg, B. O., Scheres, S. H. & Lindahl, E. Accelerated cryo-EM structure determination with parallelisation using GPUs in RELION-2. *Elife* **5**, e18722 (2016).
58. Pettersen, E. F. et al. UCSF Chimera–a visualization system for exploratory research and analysis. *J. Comput. Chem.* **25**, 1605–1612 (2004).
59. Kelley, L. A., Mezulis, S., Yates, C. M., Wass, M. N. & Sternberg, M. J. The Phyre2 web portal for protein modeling, prediction and analysis. *Nat. Protoc.* **10**, 845–858 (2015).
60. Emsley, P. & Cowtan, K. Coot: model-building tools for molecular graphics. *Acta Crystallogr. D Biol. Crystallogr.* **60**, 2126–2132 (2004).
61. Adams, P. D. et al. PHENIX: building new software for automated crystallographic structure determination. *Acta Crystallogr. D Biol. Crystallogr.* **58**, 1948–1954 (2002).
62. Amunts, A. et al. Structure of the yeast mitochondrial large ribosomal subunit. *Science* **343**, 1485–1489 (2014).
63. Chen, V. B. et al. MolProbity: all-atom structure validation for macromolecular crystallography. *Acta Crystallogr. D Biol. Crystallogr.* **66**, 12–21 (2009).
64. DeLano, W. L. The PyMOL molecular graphics system. http://pymol.org (2002).
65. Goddard, T. D. et al. UCSF ChimeraX: meeting modern challenges in visualization and analysis. *Protein Sci.* **27**, 14–25 (2018).
66. Yang, B. et al. Identification of cross-linked peptides from complex samples. *Nat. Methods* **9**, 904–906 (2012).